Astronomy Unit
School of Physics and Astronomy
Queen Mary, University of London

Precision Cosmology with the Galaxy Bispectrum

Eline Maaike de Weerd

Supervised by Dr. Chris Clarkson & Dr. Alkistis Pourtsidou

Submitted in partial fulfillment of the requirements of the Degree of
Doctor of Philosophy

Declaration

I, Eline Maaike de Weerd, confirm that the research included within this thesis is my own work or that where it has been carried out in collaboration with, or supported by others, that this is duly acknowledged below and my contribution indicated. Previously published material is also acknowledged below.

I attest that I have exercised reasonable care to ensure that the work is original, and does not to the best of my knowledge break any UK law, infringe any third party's copyright or other Intellectual Property Right, or contain any confidential material.

I accept that the College has the right to use plagiarism detection software to check the electronic version of the thesis.

I confirm that this thesis has not been previously submitted for the award of a degree by this or any other university. The copyright of this thesis rests with the author and no quotation from it or information derived from it may be published without the prior written consent of the author.

Details of collaboration and publications:

Signature: Eline Maaike de Weerd
Date: xx.xx.2021

Abstract

In this thesis, we discuss

Acknowledgements

Round up the usual suspects

Contents

Abstract **i**

Acknowledgements **ii**

1. Dipole of the Galaxy Bispectrum **1**

2. Multipoles of the Bispectrum **11**

A. First Appendix **22**

B. Second Appendix **23**
B.1. Appendix section 23

Bibliography **24**

List of Figures **26**

List of Tables **27**

1. Dipole of the Galaxy Bispectrum

The bispectrum provides an increasingly important probe of large-scale structure, complementing the information in the power spectrum and improving constraints on cosmological parameters. It has the potential to detect primordial non-Gaussianity, a key goal of large-scale galaxy surveys. The inclusion of redshift space distortions (RSD) in the bispectrum is essential for this purpose (Verde et al., 1998; Scoccimarro et al., 1999). Though this adds complexity, this means that more information can potentially be extracted (Tellarini et al., 2016).

The dominant RSD effect on galaxy number counts at first order is given by $\delta_g(\boldsymbol{k}) = (b_1 + f\mu^2)\delta(\boldsymbol{k})$, where $\mu = \boldsymbol{n}\cdot\hat{\boldsymbol{k}}$, with $\boldsymbol{n}$ the line of sight direction, f the growth rate, and b_1 is the linear bias (we omit the dependence on redshift here and below for convenience). The leading correction to this effect is a Doppler term (Kaiser, 1987; McDonald, 2009; Challinor & Lewis, 2011) (see also Raccanelli et al. (2018); Hall & Bonvin (2017); Abramo & Bertacca (2017)) proportional to $\boldsymbol{v}\cdot\boldsymbol{n}$, where $\boldsymbol{v}$ is the peculiar velocity:[1]

$$\delta_g(\boldsymbol{x}) = b_1\delta(\boldsymbol{x}) - \frac{1}{\mathcal{H}}\partial_r(\boldsymbol{v}\cdot\boldsymbol{n}) + A\,\boldsymbol{v}\cdot\boldsymbol{n} \quad \to \tag{1.1}$$

$$\delta_g(\boldsymbol{k}) = \Big(b_1 + f\mu^2 + \mathrm{i}\,A\,f\mu\frac{\mathcal{H}}{k}\Big)\delta(\boldsymbol{k})\,, \tag{1.2}$$

where $A = b_\mathrm{e} + 3\Omega_m/2 - 3 + (2-5s)(1-1/r\mathcal{H})$. Here $b_\mathrm{e} = \partial(a^3\bar{n}_g)/\partial\ln a$ is the evolution of comoving galaxy number density, $s = -(2/5)\partial\ln\bar{n}_g/\partial\ln L$ is the magnification bias (L is the threshold luminosity), r is the comoving radial distance ($\partial_r = \boldsymbol{n}\cdot\boldsymbol{\nabla}$) and we have assumed a ΛCDM background ($\mathcal{H}'/\mathcal{H}^2 = 1 - 3\Omega_m/2$, where $\mathcal{H}$ is the conformal Hubble rate, a prime is differentiation with respect to conformal time, Ω_m is the evolving density contrast). In the Fourier space expression (1.2) we can read off the relative contribution of each term by how they scale

[1] Challinor & Lewis (2011) provides the relativistic correction to the coefficient of $\boldsymbol{v}\cdot\boldsymbol{n}$ given in Kaiser (1987); McDonald (2009).

with k: terms like $\mathcal{H}/k$ are suppressed on small scales when $\mathcal{H}/k \ll 1$ but become important around and above the equality scale.

Although the galaxy density contrast (1.2) is complex, the power spectrum is real:

$$\langle \delta_g(\boldsymbol{k})\delta_g(-\boldsymbol{k})\rangle = \left[\left(b_1 + f\mu^2\right)^2 + \left(A\, f\mu\frac{\mathcal{H}}{k}\right)^2\right]\langle \delta(\boldsymbol{k})\delta(-\boldsymbol{k})\rangle\,,$$

since $\mu_{-\boldsymbol{k}} = -\mu_{\boldsymbol{k}}$ enforces a cancellation of the imaginary part, and the RSD contribution is separate from the Doppler term. However, if we consider the cross-power spectrum for *two* matter tracers, this cancellation breaks down and there is an imaginary part in the cross-power (McDonald, 2009; Bonvin, 2014):

$$\begin{aligned} P_{g\tilde{g}}(k) = \Big\{ &\Big[\left(b_1 + f\mu^2\right)\left(\tilde{b}_1 + f\mu^2\right) + A\tilde{A}f^2\mu^2\frac{\mathcal{H}^2}{k^2}\Big] \\ &+ \mathrm{i}\, f\mu\Big[\left(\tilde{b}_1 + f\mu^2\right)A - \left(b_1 + f\mu^2\right)\tilde{A}\Big]\frac{\mathcal{H}}{k}\Big\}P(k)\,. \end{aligned}$$

While the Doppler contribution to P_g is $O((\mathcal{H}/k)^2)$, the Doppler contribution to $P_{g\tilde{g}}$ mixes with the density and RSD to give an additional less suppressed part, i.e. $O(\mathcal{H}/k)$. The nonzero multipoles of P_g are $\ell = 0, 2, 4$, whereas $P_{g\tilde{g}}$ has a nonzero dipole (as well as an octupole). There are also further relativistic corrections to this dipole part of the cross power spectrum (Di Dio & Seljak, 2019).

A natural question is: what about the galaxy bispectrum? In the standard 'Newtonian' approximation, with only RSD, the galaxy bispectrum for a single tracer at fixed redshift has no dipole, and only has even multipoles (Scoccimarro et al., 1999; Nan et al., 2018). But with a lightcone corrected galaxy density contrast, the 3-point correlator, even for a *single* tracer, will no longer be an even function of $\boldsymbol{k}_a \cdot \boldsymbol{n}\,(a = 1, 2, 3)$. In order to compute the consequent contribution to the galaxy bispectrum, (1.1) is not sufficient: we need its second-order generalisation, $\delta_g \to \delta_g + \delta_g^{(2)}/2$.

Relativistic contributions to the galaxy bispectrum

At second order, the Doppler correction in (1.1) generalises to $A\,\boldsymbol{v}^{(2)} \cdot \boldsymbol{n}$, but there are also quadratic coupling terms. The couplings involve not only the Doppler effect but also radial gradients of the potential ('gravitational redshift'), volume distortion effects, and second-order corrections to the density contrast. Most of these contributions are small, but those that scale as $(\mathcal{H}/k)\delta^2$ are not, even on equality scales. Except on super-equality scales we can often neglect any terms $O((\mathcal{H}/k)^2)$ and higher, which makes the calculation considerably simpler.

1. Dipole of the Galaxy Bispectrum

The leading correction can be extracted from the general expressions that include all relativistic corrections to the Newtonian approximation, as given in Bertacca (2015) (see also Bertacca et al. (2014a); Yoo & Zaldarriaga (2014); Di Dio et al. (2014); Jolicoeur et al. (2017); Di Dio & Seljak (2019)):

$$\delta^{(2)}_{g\mathrm{D}} = A\,\boldsymbol{v}^{(2)}\cdot\boldsymbol{n} + 2C(\boldsymbol{v}\cdot\boldsymbol{n})\delta + 2\frac{E}{\mathcal{H}}(\boldsymbol{v}\cdot\boldsymbol{n})\partial_r(\boldsymbol{v}\cdot\boldsymbol{n}) \\ + 2\frac{b_1}{\mathcal{H}}\phi\,\partial_r\delta + \frac{2}{\mathcal{H}^2}\left[\boldsymbol{v}\cdot\boldsymbol{n}\,\partial_r^2\phi - \phi\,\partial_r^2(\boldsymbol{v}\cdot\boldsymbol{n})\right] - \frac{2}{\mathcal{H}}\partial_r(\boldsymbol{v}\cdot\boldsymbol{v}), \tag{1.3}$$

where ϕ is the gravitational potential, $C = b_1(A+f)+b_1'/\mathcal{H}+2(1-1/r\mathcal{H})\partial b_1/\partial\ln L$ and $E = 4-2A-\frac{3}{2}\Omega_m$. (This is in agreement with the independent re-derivation of the leading correction given in Di Dio & Seljak (2019). We have corrected a typo in the last bracket of line 1 of Eq. (2.15): $-f_{\mathrm{evo}} \to -2f_{\mathrm{evo}} \equiv -2b_{\mathrm{e}}$. Note that our $\boldsymbol{n}$ is minus theirs, and they use the convention $\delta_g + \delta_g^{(2)}$.) All but one of the contributions to this leading term contain Doppler contributions, so we label these terms with a D subscript. In this sense they can be thought of as the relativistic correction to redshift space distortions, but their origin is considerably more subtle than in the Newtonian picture (Bertacca et al., 2014a; Di Dio & Seljak, 2019). These relativistic corrections all arise as projections along the line of sight $\boldsymbol{n}$. It is this projection that is responsible for the dipole in the observed bispectrum. Beyond these leading terms in (1.3) there are a host of local coupled terms which appear on larger scales. We follow most work on the Fourier bispectrum and neglect the effect of lensing magnification. This is reasonable for correlations at the same redshift and when using very thin redshift bins allowed by spectroscopic surveys (Di Dio et al., 2019). We also use the standard plane-parallel approximation, which is reasonable on ultra-large scales. However, we note that wide-angle effects in the power spectrum can be of the same order of magnitude as the Doppler-type effects in certain circumstances (Tansella et al., 2018), and these should be incorporated in a more complete treatment.

The galaxy bispectrum is defined in Fourier space by

$$B_g(\boldsymbol{k}_1,\boldsymbol{k}_2,\boldsymbol{k}_3) = \mathcal{K}(\boldsymbol{k}_1)\mathcal{K}(\boldsymbol{k}_2)\mathcal{K}^{(2)}(\boldsymbol{k}_1,\boldsymbol{k}_2,\boldsymbol{k}_3)P(k_1)P(k_2) \\ + 2\text{ cyclic permutations}\,. \tag{1.4}$$

The first-order kernel $\mathcal{K} = \mathcal{K}_{\mathrm{N}} + \mathcal{K}_{\mathrm{D}}$ is given by the term in brackets in (1.2). At

second order, $\mathcal{K}^{(2)} = \mathcal{K}^{(2)}_{\rm N} + \mathcal{K}^{(2)}_{\rm D}$, where the Newtonian kernel is (Verde et al., 1998)

$$\mathcal{K}^{(2)}_{\rm N} = b_2 + b_1 F_2 - \frac{2}{7}(b_1 - 1)S_2 + f\, G_2 \mu_3^2 + \mathcal{Z}_2\,. \tag{1.5}$$

Here $F_2(\boldsymbol{k}_1, \boldsymbol{k}_2, \boldsymbol{k}_3), G_2(\boldsymbol{k}_1, \boldsymbol{k}_2, \boldsymbol{k}_3)$ are the second-order density and velocity kernels, and $\mathcal{Z}_2(\boldsymbol{k}_1, \boldsymbol{k}_2, \boldsymbol{k}_3)$ is the second-order RSD kernel. We use a local bias model (Desjacques et al., 2018), which includes tidal bias with kernel $S_2(\boldsymbol{k}_1, \boldsymbol{k}_2, \boldsymbol{k}_3)$. The kernels are given in Tellarini et al. (2016).

The Doppler correction to (1.5) in Fourier space follows from (1.3) (Jolicoeur et al., 2018):

$$\begin{aligned}\mathcal{K}^{(2)}_{\rm D}(\boldsymbol{k}_1, \boldsymbol{k}_2, \boldsymbol{k}_3) = {\rm i}\,\mathcal{H}\Bigg[&-\frac{3}{2}\left(\mu_1 \frac{k_1}{k_2^2} + \mu_2 \frac{k_2}{k_1^2}\right)\Omega_m b_1 + 2\mu_{12}\left(\frac{\mu_1}{k_2} + \frac{\mu_2}{k_1}\right) f^2 + \left(\frac{\mu_1}{k_1} + \frac{\mu_2}{k_2}\right) C f \\ &- \frac{3}{2}\left(\mu_1^3 \frac{k_1}{k_2^2} + \mu_2^3 \frac{k_2}{k_1^2}\right)\Omega_m f + \mu_1\mu_2\left(\frac{\mu_1}{k_2} + \frac{\mu_2}{k_1}\right)\Big(\frac{3}{2}\Omega_m - Ef\Big) f + \frac{\mu_3}{k_3} G_2(\boldsymbol{k}_1, \boldsymbol{k}_2, \boldsymbol{k}_3\end{aligned} \tag{1.6}$$

where $\mu_{ab} = \hat{\boldsymbol{k}}_a \cdot \hat{\boldsymbol{k}}_b$ and $\mu_a = \hat{\boldsymbol{k}}_a \cdot \boldsymbol{n}$. The Newtonian kernel (1.5) scales as $(\mathcal{H}/k)^0$, while the Doppler kernel (1.6) scales as $(\mathcal{H}/k)$. Using (1.5) and (1.6) in (1.4), and dropping terms that scale as $(\mathcal{H}/k)^2$ and $(\mathcal{H}/k)^3$, we find that

$$B_{g\rm N}(\boldsymbol{k}_1, \boldsymbol{k}_2, \boldsymbol{k}_3) = \mathcal{K}_{\rm N}(\boldsymbol{k}_1)\mathcal{K}_{\rm N}(\boldsymbol{k}_2)\mathcal{K}^{(2)}_{\rm N}(\boldsymbol{k}_1, \boldsymbol{k}_2, \boldsymbol{k}_3)\, P(k_1)P(k_2) + 2 \text{ cyclic permutations}\,, \tag{1.7}$$

$$B_{g\rm D}(\boldsymbol{k}_1, \boldsymbol{k}_2, \boldsymbol{k}_3) = \qquad + \Big[\mathcal{K} \tag{1.8}$$

Since (1.6) scales as $\mathcal{H}/k$ it is purely imaginary, as all these contributions have at least one $\boldsymbol{k}$ projected along the line of sight – i.e., they contain odd powers of μ_a's. This means that *the leading relativistic correction in the observed galaxy Fourier bispectrum of a single tracer is a purely imaginary addition to the Newtonian approximation.* On larger scales, terms $O((\mathcal{H}/k)^2)$ and higher appear in both the real and imaginary parts, with the kernels given in Umeh et al. (2017); Jolicoeur et al. (2017, 2018, 2019). (We include these in our plots below.)

Extracting the dipole

The bispectrum can be considered as a function of $k_1, k_2, k_3, \mu_1, \mu_2, \mu_3$ and φ, which is the azimuthal angle giving the orientation of the triangle relative to $\boldsymbol{n}$. In order to extract the dipole it is easiest to write $\mu_3 = -(k_1\mu_1 + k_2\mu_2)/k_3$, so that we can write $B_g = \sum_{i,j} \mathcal{B}_{ij}(\mathrm{i}\,\mu_1)^i(\mathrm{i}\,\mu_2)^j$, where $i, j = 0 \ldots 6$ which factors out the angular dependence multiplying real coefficients $\mathcal{B}_{ij}$ with no angular dependence. Then, use the identity $\mu_2 = \mu_1 \cos\theta + \sqrt{1-\mu_1^2}\,\sin\theta\,\cos\varphi$, where $\theta = \theta_{12}$ (and we define $\mu = \cos\theta$ – note that θ is the angle outside the triangle as the $\boldsymbol{k}_a$'s are head-to-tail). We use standard orthonormal spherical harmonics with the triangle lying in the $y-z$ plane, with $\boldsymbol{k}_1$ aligned along the z-axis (Nan et al., 2018). Then we have $Y_{\ell m}(\mu_1, \varphi)$, so that we can write $B_g = \sum_{\ell m} B_{\ell m} Y_{\ell m}(\mu_1, \varphi)$. The leading relativistic terms we consider here generate odd-power multipoles up to $\ell = 7$, and the full expression generates even and odd multipoles up to $\ell = 8$. Different powers of $(\mathrm{i}\,\mu_1)$ and $(\mathrm{i}\,\mu_2)$ contribute to the dipole,

$$\int \mathrm{d}\Omega(\mathrm{i}\,\mu_1)^i(\mathrm{i}\,\mu_2)^j Y^*_{1m} = \delta_{m,0}\frac{\mathrm{i}\sqrt{3\pi}}{15}\begin{bmatrix} 0 & 10\mu & 0 & -6\mu & \\ 10 & 0 & -4\mu^2-2 & 0 & \cdots \\ 0 & -6\,\mu & 0 & \frac{12\mu^3+18\mu}{7} & \\ -6 & 0 & \frac{24\,\mu^2+6}{7} & 0 & \\ & \vdots & & & \ddots \end{bmatrix} + \delta_{m,\pm1}\frac{\sqrt{6\pi}}{15}\begin{bmatrix} 0 & -5 & 0 & \\ 0 & 0 & 2\,\mu & \\ 0 & 1 & 0 & -\frac{6}{} \\ 0 & 0 & -\frac{6}{7}\,\mu & \\ & \vdots & & \end{bmatrix} \tag{1.9}$$

where each matrix element corresponds to a particular combination of i, j, where the matrix indices run over the values $i = 0 \ldots 6, j = 0 \ldots 6$, with powers above 3 not written above; these are polynomials in μ up to order 6. From this we can read off the terms from $\mathcal{K}_\mathrm{D}$ contribute to differing $m = 0, \pm 1$. In particular, if $i + j$ is even – i.e., the real part of the bispectrum – there is no contribution: only the imaginary terms, corresponding to $i + j$ odd, contribute. For the monopole, only $i + j$ even contribute. Therefore, at $O(\mathcal{H}/k)$, *the monopole of the bispectrum is the Newtonian part, while the dipole is purely from the relativistic corrections. The presence of the dipole is therefore a 'smoking gun' signal for the leading relativistic correction to the bispectrum.* At order $O((\mathcal{H}/k)^2)$, relativistic terms appear in the monopole, which were considered in Umeh et al. (2017); Jolicoeur et al. (2017, 2018, 2019).

Squeezed, equilateral and flattened limits

It is relatively straightforward to understand the type of dipole generated in different triangular configurations in our conventions. In particular, for the $O(\mathcal{H}/k)$ relativistic dipole:

- The squeezed case is zero for $m = 0$, and is non-zero for $m = \pm 1$. We see this directly from (1.9): with $\mu = -1$ the $m = 0$ contribution is anti-symmetric in i, j while $\mathcal{B}_{ij}$ is symmetric in this limit.
- In the equilateral case, the dipole is zero (this is the case for all orders in $\mathcal{H}/k$).
- The flattened case ($k_1 = k_2 = k_3/2, \theta = 0$) is zero for $m = \pm 1$ (for all orders in $\mathcal{H}/k$), but is non-zero for $m = 0$. This can be seen directly from (1.9) with $\theta = 0$.

To show the equilateral case is zero is a lengthy calculation involving many cancellations. Let us illustrate instead the squeezed case. We write $k_1 = k_2 = \sqrt{1+\varepsilon^2}k_S, k_3 = 2\varepsilon k_S$. In this case the triangle has small angle 2ε and equal angles $\pi/2 - \varepsilon$, where the squeezed limit is $\varepsilon \to 0$. It is convenient to replace $(1, 2, 3)$ by $(S, -S, L)$. Then to $O(\varepsilon)$, $k_{-S} = k_S\,, \quad k_L = 2\varepsilon k_S\,, \quad \mu_{-S} = -\mu_S - 2\varepsilon\mu_L\,, \mu_L = -\sqrt{1-\mu_S^2}\,\cos\varphi - \varepsilon\mu_S$. In this limit, the permutations of the relativistic kernels become

$$\mathcal{K}_{\rm D}^{(2)}(\boldsymbol{k}_L, \boldsymbol{k}_S, \boldsymbol{k}_{-S}) = \mathrm{i}\,\mathcal{H}\Big[-\frac{3}{2}\Omega_m b_1 \mu_S \frac{k_S}{k_L^2} + Cf\frac{\mu_L}{k_L} \\ -\frac{3}{2}\Omega_m f\mu_S^3\frac{k_S}{k_L^2} + \Big(\frac{3}{2}\Omega_m - Ef\Big) f\mu_S^2\frac{\mu_L}{k_L}\Big] \tag{1.10}$$

and $\mathcal{K}_{\rm D}^{(2)}(\boldsymbol{k}_{-S}, \boldsymbol{k}_L, \boldsymbol{k}_S) = \mathcal{K}_{\rm D}^{(2)}(\boldsymbol{k}_L, \boldsymbol{k}_S, \boldsymbol{k}_{-S})\big|_{\mu_S \to \mu_{-S}}$ while $\mathcal{K}_{\rm D}^{(2)}(\boldsymbol{k}_S, \boldsymbol{k}_{-S}, \boldsymbol{k}_L) = 0$. In the squeezed limit of the cyclic sum (1.4), the terms $\mathcal{K}^{(2)}(\boldsymbol{k}_L, \boldsymbol{k}_S, \boldsymbol{k}_{-S})$ and $\mathcal{K}^{(2)}(\boldsymbol{k}_{-S}, \boldsymbol{k}_L, \boldsymbol{k}_S)$ appear only in the form $\mathcal{K}^{(2)}(\boldsymbol{k}_L, \boldsymbol{k}_S, \boldsymbol{k}_{-S}) + \mathcal{K}^{(2)}(\boldsymbol{k}_{-S}, \boldsymbol{k}_L, \boldsymbol{k}_S)$. This sum regularises the divergent $k_S/k_L = (2\varepsilon)^{-1}$ and $k_S/k_L^2 = (2\varepsilon k_L)^{-1}$ terms. We obtain the bispectrum in the squeezed limit,

$$B_g^{\rm sq} = b_{1S}b_{1L}b_{SL}\,P_L P_S + \mathrm{i}\,b_{1S}\Big\{b_{SL}fA + \frac{3}{2}\Omega_m b_{1S}b_{1L} \\ + 2b_{1L}fC + b_{1L}\mu_S^2\Big[\frac{3}{2}\Omega_m - Ef\Big]\Big\} P_L P_S\,\mu_L\frac{\mathcal{H}}{k_L}\,, \tag{1.11}$$

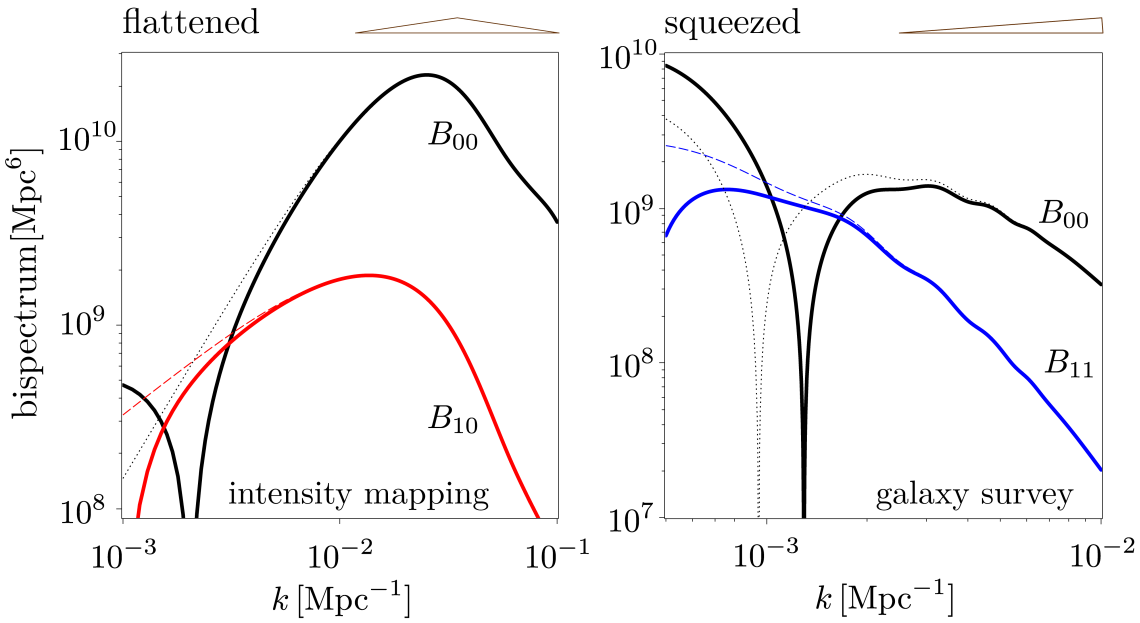

Figure 1.1.: The absolute value of the bispectrum dipole at $z = 1$ as a function of triangle size, in the flattened (Left, $\theta = 2°$, for intensity mapping bias) and squeezed (Right, $\theta = 178°$, for Euclid-like bias) configurations, with k_3 as the horizontal axis. Red is the $m = 0$ part and blue is $m = \pm 1$. Dashed (and dotted) lines show up to the $O(\mathcal{H}/k)$ terms considered analytically here, while solid lines indicate larger-scale contributions. For reference the monopole is in black, with the dotted line the Newtonian part. (The zero-crossing in the monopole for the squeezed case is a result of the tidal bias.)

where $P_{S,L} = P(k_{S,L})$, $b_{1S,L} \equiv b_1 + f\mu^2_{S,L}$ and

$$b_{SL} \equiv 2b_2 + \frac{43}{21}b_1 - \frac{4}{21} + \left(2b_1 + \frac{5}{7}\right) f\mu_S^2 + f\mu_L^2 b_{1S}\,.$$

Note that only the first term in the squeezed bispectrum comes from the Newtonian limit.

The type of dipole extracted from this term is seen as follows. To this order we can write $\mu_S^2 = \mu_S\mu_{-S}$. Then, since $\mu_L = -2(\mu_S + \mu_{-S})/\varepsilon$, we see that the $m = 0$ term is zero because $B^{\rm sq}_{g\rm D}$ is symmetric in $\mu^i_S\mu^j_{-S}$ under $i \leftrightarrow j$, while the $m = 0$ term is antisymmetric in (1.9). This leaves just the $m = \pm 1$ contribution in (1.9).

The dipole in intensity mapping and galaxy surveys

We now consider the amplitude of the dipole relevant for upcoming galaxy surveys, which have different bias parameters. We consider two different types of

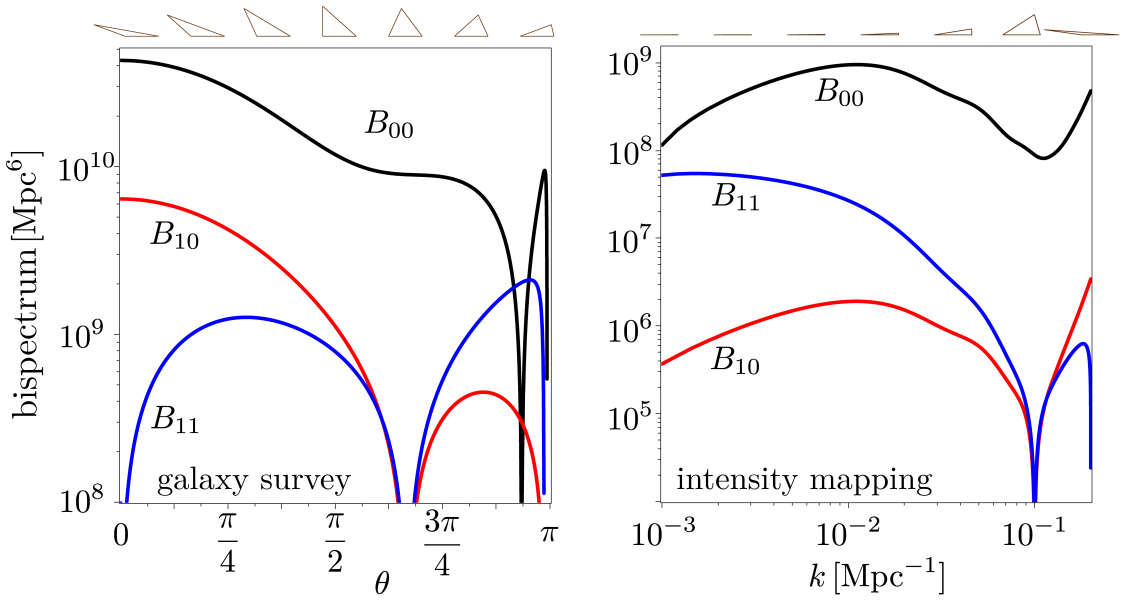

Figure 1.2.: (Left) We show the dipoles as a function of θ with a bias appropriate for a Euclid-like survey, for $k_1 = k_2 = 0.01\,\mathrm{Mpc}^{-1}$. The left of the plot corresponds to the flattened case where the $m = 0$ (red) dipole reaches 10% of the monopole. (Right) We show the IM signal with $k_1 = k_2 = 0.1\,\mathrm{Mpc}^{-1}$ versus the long mode k_3. Except for very long modes $\theta \approx \pi$, our $O(\mathcal{H}/k)$ truncation is a very good approximation in these examples.

survey: an SKA intensity mapping of 21 cm radio emission, as well as a Euclid-like optical/infrared spectroscopic survey. An intensity map of the 21cm emission of neutral hydrogen (HI) in the post-reionization Universe records the total emission in galaxies containing HI, without detecting individual galaxies. There is an equivalence between the brightness temperature contrast and number count contrast (Umeh et al., 2016). For IM we use the bias parameters at $z = 1$, $b_1 = 0.856, b_2 = -0.321, b_1' = -0.5 \times 10^{-4}, b_e = -0.5, b_e' = 0, s = 2/5$ (Fonseca et al., 2018; Umeh et al., 2016) while for the spectroscopic survey we use $b_1 = 1.3, b_2 = -0.74, b_1' = -1.6 \times 10^{-4}, b_e = -4, b_e' = 0, s = -0.95$ (Camera et al., 2018; Yankelevich & Porciani, 2019). For intensity mapping, $\partial b_1/\partial lnL = 0$ and we assume it is zero for simplicity for the spectroscopic survey. We use a LCDM model with standard parameters $\Omega_m = 0.314, h = 0.67, f_{\rm baryon} = 0.157, n_s = 0.968$. Plots are presented using linear power spectra generated using CAMB (Lewis et al., 2000).

In Fig. (1.1) we show how changing the scale of a fixed triangle changes the amplitude of the dipole, with reference to the monopole. In the flattened case with $m = 0$ we see the signal peaks for triangles below the equality scale, while for squeezed shapes, with $m = \pm 1$, the signal is smaller, and peaks when the long mode approaches the Hubble scale. In Fig. (1.2) we change the shape with fixed $k_1 = k_2$ for both galaxy and IM surveys. We confirm our analytical results that the equilateral limit is zero, as well as the other limits. For triangles between right-angle and flattened the dipole is more than 10% of the monopole, and the signal is largest in the flattened case – except in the extreme squeezed limit (not shown).

Conclusions

We have shown for the first time that the relativistic galaxy bispectrum has a leading correction which is a local dipole with respect to the observers line of sight. In contrast to the power spectrum, this dipole exists even for a single tracer. We have shown analytically how the dipole is generated for the leading terms, and numerically we have included all local contributions, which show up above the equality scale. We have neglected integrated terms which will also contribute to the dipole, but their inclusion in a Fourier space bispectrum is non-trivial. Local relativistic corrections will induce all multipoles up to $\ell = 8$ at every m, in contrast to the Newtonian case which only induces even $\ell = 0, 2, 4$. We will investigate these new multipoles in a forthcoming publication.

We have shown that this dipole is large with respect to the monopole in both the flattened and squeezed limits, which excite different orders of the dipole orientation

m. We have shown that even on equality scales it is about 10% of the monopole at $z = 1$ for flattened shapes which have the largest amplitude. In more squeezed cases where the short mode is $\sim 10\,\mathrm{Mpc}$ the dipole can also be a large part of the IM signal. Furthermore, although we have only considered Gaussian initial conditions here, the dipole will be unaffected by non-Gaussianity at leading order because these corrections start at $O((\mathcal{H}/k)^2)$, making our predictions relatively robust to this. This implies that the dipole of the bispectrum is a unique signature of general relativity on cosmological scales, and therefore offers a new observational window onto modifications of general relativity.

2. Multipoles of the Bispectrum

Above the equality scale the galaxy bispectrum will be a key probe for measuring primordial non-Gaussianity which can help differentiate between different inflationary models and other theories of the early universe. On these scales a variety of relativistic effects come into play once the galaxy number-count fluctuation is projected onto our past lightcone. By decomposing the Fourier-space bispectrum into invariant multipoles about the observer's line of sight we examine in detail how the relativistic effects contribute to these. We show how to perform this decomposition analytically, which is significantly faster for subsequent computations. While all multipoles receive a contribution from the relativistic part, odd multipoles arising from the imaginary part of the bispectrum have no Newtonian contribution, making the odd multipoles a smoking gun for a relativistic signature in the bispectrum for single tracers. The dipole and the octopole are significant on equality scales and above where the Newtonian approximation breaks down. This breakdown is further signified by the fact that the even multipoles receive a significant correction on very large scales.

Introduction

The bispectrum will play a key role in future galaxy surveys as an important probe of large-scale structure and for measuring primordial non-Gaussianity and galaxy bias Jeong & Komatsu (2009); Baldauf et al. (2011); Celoria & Matarrese (2020). It can help discriminate between different inflationary models and other theories of the early universe, and contains information that is complementary and additional to what is contained in the power spectrum. On super-equality scales, a variety of relativistic effects come into play once the galaxy number-count fluctuation is projected onto the past light cone. In the density contrast up to second order, relativistic effects arise from observing on the past lightcone, and they include all redshift, volume and lensing distortions and couplings between these. In Poisson gauge, these effects can be attributed to velocities (Doppler), gravitational potentials (Sachs-Wolfe, integrated SW, time delay) and lensing magnification and shear. In addition, there

are corrections arising from a GR definition of galaxy bias Bertacca et al. (2014b). These effects generate corrections to the Newtonian approximation at order $\mathcal{O}(\mathcal{H}/k)$ and higher. Non-Gaussianity generated by these relativistic projection effects could closely mimic the signature of $f_{\rm NL}$ on large scales which gives a correction in the halo bias $\mathcal{O}((\mathcal{H}/k)^2)$, indicating the importance of precisely including all $\mathcal{O}(\mathcal{H}/k)$ and higher effects in theoretical modelling. So far, a variety of relativistic effects in the galaxy Fourier bispectrum has been taken into account, see Umeh et al. (2017); Jolicoeur et al. (2017, 2018, 2019); Clarkson et al. (2019); Maartens et al. (2020) under the assumption of the plane parallel approximation, and neglecting integrated effects. Other groups are working on this from different angles and approaches, for example by a spherical-Fourier formalism Bertacca et al. (2018), and calculating the angular galaxy bispectrum Di Dio et al. (2017, 2019). Crucially, we have shown that the relativistic part should be detectable in a survey like Euclid without resorting to the multi-tracer technique, which is needed for the power spectrum Maartens et al. (2020) .

Once an observable like the galaxy number-count fluctuation is projected onto the past lightcone the orientation of the triangle in the Fourier space bispectrum becomes important. Analogously to how the Legendre multipole expansion is used for power spectrum analysis, one can expand the galaxy bispectrum in spherical harmonics, thus isolating the different invariant multipoles with respect to the observer's line of sight $\boldsymbol{n}$. We use the full spherical harmonics for the bispectrum rather than the Legendre polynomial expansion usually adopted for the power spectrum because of the azimuthal degrees of freedom associated with the orientation of the triangle with respect to the line of sight direction vector in Fourier space. In the power spectrum limit, there is only one angular degree of freedom after ensemble averaging. For the bispectrum, we have one angular and one azimuthal degree of freedom which when expanded in spherical harmonics leads to $(2\ell + 1)$ independent harmonics for each multipole value ℓ.

This has been done for the Newtonian bispectrum, which generates non-zero multipoles only for even ℓ (up to $\ell = 8$) due to redshift-space distortions Scoccimarro et al. (1999); Nan et al. (2018). Contrary to the Newtonian bispectrum, the relativistic galaxy bispectrum generates non-zero multipoles for both even and odd ℓ up to $\ell = 8$ and $m = 6$ where the odd multipoles are induced by the general relativistic effects only. This means that these multipoles are a crucial signature of relativistic projection effects. We provide, for the first time, a multipole decomposition of the Fourier space galaxy bispectrum with relativistic effects included. Additionally we show that the coefficients of this expansion can be worked out analytically. We

provide an exact analytic formula for this multipole expansion of the galaxy bispectrum. Previously, we examined for the first time the dipole of the galaxy bispectrum in detail, showing that its amplitude can be more than 10% of that of the monopole even at equality scales Clarkson et al. (2019). In order to eliminate possible biases when analysing large scale structure data, it is important to include the relativistic effects. In addition to this, a variety of the effects that appear in the bispectrum are relativistic effects that have not been measured elsewhere and hence are interesting to study. By analysing the non-zero multipoles of the galaxy bispectrum both for a Euclid-like galaxy survey, and for an SKA-like HI intensity mapping survey, we show the behaviour of the higher multipoles and their corrections to the Newtonian bispectrum. In follow-up work, we are investigating possibilities of detecting the higher multipoles of the bispectrum. See for example Maartens et al. (2020) for detection prospects of the leading order relativistic effects; the dipole is expected to have the strongest GR signature.

The paper is organised as follows. We introduce the relativistic Fourier space bispectrum in section 2, and present the multipole expansion of the relativistic bispectrum in section 2. An analysis of the multipoles can be found in section 2. Finally, we summarise our conclusions in section 2.

The relativistic bispectrum

In Fourier space, the observed galaxy bispectrum B_g at a fixed redshift z is given by Jolicoeur et al. (2017, 2018)

$$\langle \Delta_g(z,\boldsymbol{k}_1)\Delta_g(z,\boldsymbol{k}_2)\Delta_g(z,\boldsymbol{k}_3)\rangle = (2\pi)^3 B_g(z,\boldsymbol{k}_1,\boldsymbol{k}_2,\boldsymbol{k}_3)\delta^D(\boldsymbol{k}_1+\boldsymbol{k}_2+\boldsymbol{k}_3), \qquad (2.1)$$

where $\Delta_g(z,\boldsymbol{k}_1)$ is the number count contrast at redshift z (see Jolicoeur et al. (2017) for the full expression). Here we work in the Poisson gauge; note that $\Delta_g = \delta_g + \text{RSD} + \text{GR projection effects}$, where the RSD term is the Kaiser RSD up to second order, which is part of the Newtonian approximation. Since redshift is fixed, in what follows we drop redshift dependence for brevity. Furthermore, since the observed direction $\boldsymbol{n}$ is fixed in what follows, the plane-parallel approximation is necessarily assumed. Then, at tree level, and for Gaussian initial conditions, the following combinations of terms contribute,

$$\langle \Delta_g(\boldsymbol{k}_1)\Delta_g(\boldsymbol{k}_2)\Delta_g(\boldsymbol{k}_3)\rangle = \frac{1}{2}\langle \Delta_g^{(1)}(\boldsymbol{k}_1)\Delta_g^{(1)}(\boldsymbol{k}_2)\Delta_g^{(2)}(\boldsymbol{k}_3)\rangle + 2 \text{ cyclic permutations}. \qquad (2.2)$$

Using Wick's theorem, this gives an expression for the galaxy bispectrum Jolicoeur et al. (2017)

$$B_g(\boldsymbol{k}_1,\boldsymbol{k}_2,\boldsymbol{k}_3) = \mathcal{K}^{(1)}(\boldsymbol{k}_1)\mathcal{K}^{(1)}(\boldsymbol{k}_2)\mathcal{K}^{(2)}(\boldsymbol{k}_1,\boldsymbol{k}_2,\boldsymbol{k}_3)P(\boldsymbol{k}_1)P(\boldsymbol{k}_2) + 2 \text{ cyclic permutations}, \tag{2.3}$$

where P is the power spectrum of $\delta^{(1)}_{\rm T}$, the first order dark matter density contrast in the total-matter gauge, which corresponds to an Eulerian frame. The first order kernel can be split into a Newtonian and a relativistic part as Jeong et al. (2012)

$$\mathcal{K}^{(1)} = \mathcal{K}^{(1)}_{\rm N} + \mathcal{K}^{(1)}_{\rm GR}, \qquad \mathcal{K}^{(1)}_{\rm N} = b_1 + f\mu^2, \qquad \mathcal{K}^{(1)}_{\rm GR} = \mathrm{i}\,\mu\frac{\gamma_1}{k} + \frac{\gamma_2}{k^2}, \tag{2.4}$$

with $\mu = \hat{\boldsymbol{k}}\cdot\boldsymbol{n}$ ($\hat{\boldsymbol{k}} = \boldsymbol{k}/k$), b_1 is the first-order Eulerian galaxy bias coefficient, f is the linear growth rate of matter perturbations, and redshift-dependent coefficients γ_i are Jeong et al. (2012),

$$\frac{\gamma_1}{\mathcal{H}} = f\left[b_e - 2\mathcal{Q} - \frac{2(1-\mathcal{Q})}{\chi\mathcal{H}} - \frac{\mathcal{H}'}{\mathcal{H}^2}\right], \tag{2.5}$$

$$\frac{\gamma_2}{\mathcal{H}^2} = f(3-b_e) + \frac{3}{2}\Omega_m\left[2 + b_e - f - 4\mathcal{Q} - \frac{2(1-\mathcal{Q})}{\chi\mathcal{H}} - \frac{\mathcal{H}'}{\mathcal{H}^2}\right]. \tag{2.6}$$

In equations (2.5) and (2.6), $\mathcal{H}$ is the conformal Hubble rate $(\ln a)'$, where a prime denotes a derivative with respect to conformal time; b_e and $\mathcal{Q}$ are the galaxy evolution and magnification biases respectively, χ is the line-of-sight comoving distance and $\Omega_m = \Omega_{m0}(1+z)H_0^2/\mathcal{H}^2$ is the matter density parameter. At first order, the gauge-independent GR definition of galaxy bias is made in the common comoving frame of galaxies and matter,

$$\delta^{(1)}_{g\rm C} = b_1\delta^{(1)}_{\rm C} = b_1\delta^{(1)}_{\rm T}\,, \tag{2.7}$$

where subscript C is for the comoving gauge and T is for total matter gauge, which is a gauge corresponding to standard Newtonian perturbation theory. The bias relation in Poisson gauge is then obtained by transforming (2.7) to Poisson gauge Bertacca et al. (2014b); Jolicoeur et al. (2018):

$$\delta^{(1)}_g = \delta^{(1)}_{g\rm C} + (3-b_e)\mathcal{H}v^{(1)} = b_1\delta^{(1)}_{\rm T} + (3-b_e)\mathcal{H}v^{(1)}, \tag{2.8}$$

where $v^{(1)}$ is the velocity potential. Since $v^{(1)} = f\mathcal{H}\delta^{(1)}_T/k^2$, the last term on the right of equation (2.8) leads to the $f(3-b_e)$ term in $\gamma_2/\mathcal{H}^2$, equation (2.6).

Similarly to the first order kernel, the second order kernel can be split into a

Newtonian and a relativistic part. The second order part of the Newtonian kernel is well studied and is given as Bernardeau et al. (2002); Karagiannis et al. (2018); Scoccimarro et al. (1999); Verde et al. (1998)

$$\mathcal{K}_{\rm N}^{(2)}(\boldsymbol{k}_1,\boldsymbol{k}_2,\boldsymbol{k}_3) = b_1 F_2(\boldsymbol{k}_1,\boldsymbol{k}_2) + b_2 + f\mu_3^2 G_2(\boldsymbol{k}_1,\boldsymbol{k}_2) + f Z_2(\boldsymbol{k}_1,\boldsymbol{k}_2) + b_{s^2} S_2(\boldsymbol{k}_1,\boldsymbol{k}_2), \tag{2.9}$$

where $\mu_i = \hat{\boldsymbol{k}}_i \cdot \boldsymbol{n}$, b_2 is the second-order Eulerian bias parameter, and b_{s^2} is the tidal bias. F_2 and G_2 are the Fourier-space Eulerian kernels for second-order density contrast and velocity respectively Jolicoeur et al. (2017); Villa & Rampf (2016);

$$\begin{aligned} F_2(\boldsymbol{k}_1,\boldsymbol{k}_2) &= 1 + \frac{F}{D^2} + \left(\hat{\boldsymbol{k}}_1\cdot\hat{\boldsymbol{k}}_2\right)\left(\frac{k_1}{k_2}+\frac{k_2}{k_1}\right) + \left(1-\frac{F}{D^2}\right)\left(\hat{\boldsymbol{k}}_1\cdot\hat{\boldsymbol{k}}_2\right)^2, \\ G_2(\boldsymbol{k}_1,\boldsymbol{k}_2) &= \frac{F'}{DD'} + \left(\hat{\boldsymbol{k}}_1\cdot\hat{\boldsymbol{k}}_2\right)\left(\frac{k_1}{k_2}+\frac{k_2}{k_1}\right) + \left(2-\frac{F'}{DD'}\right)\left(\hat{\boldsymbol{k}}_1\cdot\hat{\boldsymbol{k}}_2\right)^2, \end{aligned} \tag{2.10}$$

where F is a second-order growth factor, which is given by the growing mode solution of,

$$F'' + \mathcal{H}F' - \frac{3}{2}\frac{H_0^2\Omega_{m0}}{a}F = \frac{3}{2}\frac{H_0^2\Omega_{m0}}{a}D^2. \tag{2.11}$$

In an Einstein-de Sitter background, $F = 3D^2/7$, which is a very good approximation for ΛCDM which we use here. The second-order RSD part of the Newtonian kernel is comprised of G_2 above and the kernel Z_2 Verde et al. (1998); Scoccimarro et al. (1999),

$$Z_2(\boldsymbol{k}_1,\boldsymbol{k}_2) = f\frac{\mu_1\mu_2}{k_1k_2}\left(\mu_1k_1+\mu_2k_2\right)^2 + \frac{b_1}{k_1k_2}\left[\left(\mu_1^2+\mu_2^2\right)k_1k_2 + \mu_1\mu_2\left(k_1^2+k_2^2\right)\right]. \tag{2.12}$$

Finally, $S_2(\boldsymbol{k}_1,\boldsymbol{k}_2)$ is the kernel for the tidal bias,

$$S_2(\boldsymbol{k}_1,\boldsymbol{k}_2) = (\hat{\boldsymbol{k}}_1\cdot\hat{\boldsymbol{k}}_2)^2 - \frac{1}{3}. \tag{2.13}$$

The Newtonian bias model is

$$\delta_{g\rm T}^{(2)} = b_1\delta_{\rm T}^{(2)} + b_2\left[\delta_{\rm T}^{(1)}\right]^2 + b_{s^2}s^2, \tag{2.14}$$

where $s^2 = s_{ij}s^{ij}$, and $s_{ij} = \Phi_{,ij} - \delta_{ij}\nabla^2\Phi/3$.

The relativistic part of the second order kernel was first derived in Umeh et al. (2017) in the simplest case and extended in Jolicoeur et al. (2017, 2018, 2019).

Neglecting sub-dominant vector and tensor contributions, we have

$$\begin{aligned}\mathcal{K}^{(2)}_{\rm GR}(\boldsymbol{k}_1,\boldsymbol{k}_2,\boldsymbol{k}_3) = \frac{1}{k_1^2k_2^2}\Big\{&\beta_1 + E_2(\boldsymbol{k}_1,\boldsymbol{k}_2,\boldsymbol{k}_3)\beta_2 + \mathrm{i}\,(\mu_1k_1+\mu_2k_2)\beta_3 + \mathrm{i}\,\mu_3k_3\,[\beta_4 + E_2(\boldsymbol{k}_1,\boldsymbol{k}_2,\boldsymbol{k}_3)\beta\\ &+\frac{k_1^2k_2^2}{k_3^2}\left[F_2(\boldsymbol{k}_1,\boldsymbol{k}_2)\beta_6 + G_2(\boldsymbol{k}_1,\boldsymbol{k}_2)\beta_7\right] + (\mu_1k_1\mu_2k_2)\,\beta_8 + \mu_3^2k_3^2\,(\beta_9 + E_2(\boldsymbol{k}_1,\boldsymbol{k}_2,\boldsymbol{k}_3)\\ &+(\boldsymbol{k}_1\cdot\boldsymbol{k}_2)\,\beta_{11} + \left(k_1^2+k_2^2\right)\beta_{12} + \left(\mu_1^2k_1^2+\mu_2^2k_2^2\right)\beta_{13}\\ &+\mathrm{i}\left[\left(\mu_1k_1^3+\mu_2k_2^3\right)\beta_{14} + (\mu_1k_1+\mu_2k_2)\,(\boldsymbol{k}_1\cdot\boldsymbol{k}_2)\,\beta_{15} + k_1k_2\,(\mu_1k_2+\mu_2k_1)\,\beta_{16}\right.\\ &\left.+\left(\mu_1^3k_1^3+\mu_2^3k_2^3\right)\beta_{17} + \mu_1\mu_2k_1k_2\,(\mu_1k_1+\mu_2k_2)\,\beta_{18} + \mu_3\frac{k_1^2k_2^2}{k_3}G_2(\boldsymbol{k}_1,\boldsymbol{k}_2)\beta_{19}\right]\Big\}.\end{aligned} \tag{2.15}$$

We have collected terms according to the overall powers of k involved. The β_i here are redshift- and bias-dependent coefficients, given in full in appendix REF BETA APPENDIX, which updates expressions in previous papers. We have defined the kernel E_2 which scales as k^0 (like F_2, G_2, and Z_2 do),

$$E_2(\boldsymbol{k}_1,\boldsymbol{k}_2,\boldsymbol{k}_3) = \frac{k_1^2k_2^2}{k_3^4}\left[3 + 2\left(\hat{\boldsymbol{k}}_1\cdot\hat{\boldsymbol{k}}_2\right)\left(\frac{k_1}{k_2}+\frac{k_2}{k_1}\right) + \left(\hat{\boldsymbol{k}}_1\cdot\hat{\boldsymbol{k}}_2\right)^2\right], \tag{2.16}$$

which incorporates some of the relativistic dynamical corrections to the intrinsic second-order terms.

At second order, the GR bias model, which corrects the Newtonian bias model (2.14) is given by Umeh et al. (2019),

$$\delta^{(2)}_{g\mathrm{T}} = b_1\delta^{(2)}_{\mathrm{T}} + b_2\left[\delta^{(1)}_{\mathrm{T}}\right]^2 + b_{s^2}s^2 + \delta^{(2)}_{\mathrm{C,GR}}\,, \tag{2.17}$$

where the last term maintains gauge invariance on ultra-large scales, and is given by (using $\delta^{(1)}_{\mathrm{C}} = \delta^{(1)}_{\mathrm{T}}$)

$$\delta^{(2)}_{\mathrm{C,GR}} = 2\mathcal{H}^2(3\Omega_m + 2f)\left[\delta^{(1)}_{\mathrm{T}}\nabla^{-2}\delta^{(1)}_{\mathrm{T}} - \frac{1}{4}\partial_i\nabla^{-2}\delta^{(1)}_{\mathrm{T}}\partial^i\nabla^{-2}\delta^{(1)}_{\mathrm{T}}\right]. \tag{2.18}$$

The GR correction (2.18) to the Newtonian bias model is contained in the GR kernel (2.15). Then, we also need to transform $\delta^{(2)}_{g\mathrm{T}}$ to the Poisson gauge $\delta^{(2)}_g$, the expression for this is given in Jolicoeur et al. (2017),

$$\begin{aligned}\delta^{(2)}_g = \delta^{(2)}_{g\mathrm{T}} + (3-b_e)\mathcal{H}v^{(2)} + \left[(b_e-3)\mathcal{H}' + b_e'\mathcal{H} + (b_e-3)^2\mathcal{H}^2\right]\left[v^{(1)}\right]^2 + (b_e-3)\mathcal{H}v^{(1)}v^{(1)\prime}\\ + 2(3-b_e)\mathcal{H}v^{(1)}\delta^{(1)}_{g\mathrm{T}} - 2v^{(1)}\delta^{(1)\prime}_{g\mathrm{T}} + 3\,(b_e-3)\,\mathcal{H}v^{(1)}\Phi^{(1)}\,.\end{aligned} \tag{2.19}$$

All of the terms after $\delta_{g\mathrm{T}}^{(2)}$ on the right of equation (2.19) scale as $(\mathcal{H}/k)^n \left[\delta_{\mathrm{T}}^{(1)}\right]^2$, where $n = 2, 4$. Therefore they are omitted in the Newtonian approximation. These GR correction terms maintain gauge-independence on ultra-large scales, and they are included in the GR kernel (2.15).

Extracting the multipoles

Our goal is to extract the spherical harmonic multipoles of B_g with respect to the observer's line of sight. That is, for a fixed line of sight and triangle shape, the rotation of the plane of the triangle about $\boldsymbol{n}$ generates invariant moments, the sum of which add up to the full bispectrum. This means that

$$B_g = \sum_{\ell m} B_{\ell m} Y_{\ell m}(\boldsymbol{n})\,, \tag{2.20}$$

where we follow Scoccimarro et al. (1999); Nan et al. (2018) in our choice of decomposition of the bispectrum (an alternative basis can be found in Sugiyama et al. (2018)). To define the $B_{\ell m}$ we need to define an orientation for the $Y_{\ell m}$ to give the polar and azimuthal angles over which to integrate. We choose a coordinate basis for the vectors that span the triangle as follows:

$$\boldsymbol{k}_1 = (0, 0, k_1) \tag{2.21}$$

$$\boldsymbol{k}_2 = (0, k_2 \sin\theta, k_2 \cos\theta)\,, \tag{2.22}$$

$$\boldsymbol{k}_3 = (0, -k_2 \sin\theta, -k_1 - k_2 \cos\theta)\,, \tag{2.23}$$

$$\boldsymbol{n} = (\sin\theta_1 \cos\varphi, \sin\theta_1 \sin\varphi, \cos\theta_1)\,. \tag{2.24}$$

That is, we fix $\boldsymbol{k}_1$ along the z-axis, and require the other triangle vectors to lie in the y-z plane, see figure 2.1 for a sketch of the relevant vectors. Then we define $\mu_1 = \cos\theta_1$ and use φ, which is the azimuthal angle giving the orientation of the triangle relative to $\boldsymbol{n}$. $\theta_{12} = \theta$ is the angle between vectors $\boldsymbol{k}_1$ and $\boldsymbol{k}_2$, and we define $\mu = \cos\theta = \hat{\boldsymbol{k}}_1 \cdot \hat{\boldsymbol{k}}_2$.

The bispectrum can then be expressed in terms of five variables, φ, μ_1, θ, k_1 and k_2, by using

$$\mu_2 = \sqrt{1 - \mu_1^2}\sin\theta\sin\varphi + \mu_1\cos\theta\,, \tag{2.25}$$

$$\mu_3 = -\frac{k_1}{k_3}\mu_1 - \frac{k_2}{k_3}\mu_2. \tag{2.26}$$

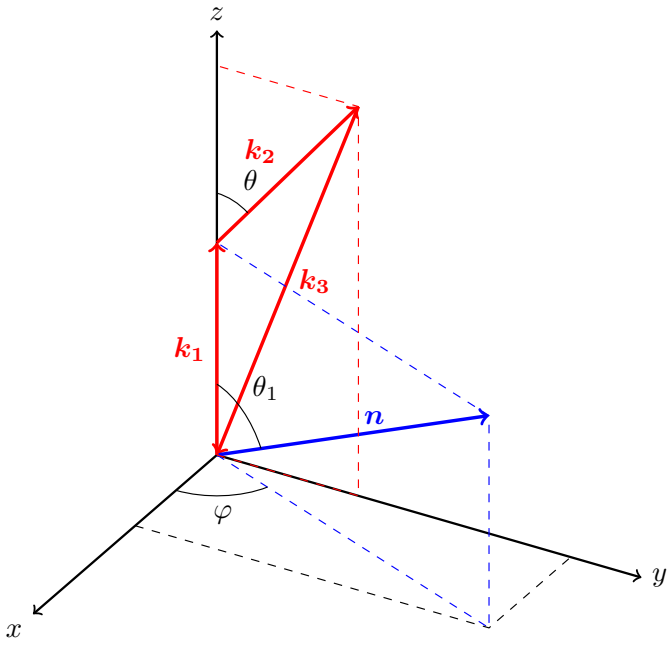

Figure 2.1.: Overview of the relevant vectors and angles for the Fourier-space bispectrum.

Then

$$B_g(\theta, k_1, k_2, \mu_1, \varphi) = \sum_{\ell m} B_{\ell m}(\theta, k_1, k_2) Y_{\ell m}(\mu_1, \varphi)\,, \tag{2.27}$$

where we use standard orthonormal spherical harmonics,

$$Y_{\ell m}(\mu_1, \varphi) = \sqrt{\frac{2\ell+1}{4\pi}} \sqrt{\frac{(\ell-m)!}{(\ell+m)!}} P_\ell^m(\mu_1) e^{\mathrm{i}\, m\varphi}, \tag{2.28}$$

where the P_ℓ^m are the associated Legendre polynomials,

$$P_\ell^m(\mu_1) = \frac{(-1)^m}{2^\ell\, \ell!} (1-\mu_1^2)^{m/2} \frac{\mathrm{d}^{\ell+m}}{\mathrm{d}\mu_1^{\ell+m}} (\mu_1^2 - 1)^\ell. \tag{2.29}$$

At this stage we can extract the multipoles numerically once a bias model and cosmological parameters are given. It is actually significantly quicker to perform this extraction algebraically however, as we now explain.

The bispectrum in general can be considered as a function of $k_1, k_2, k_3, \mu, \mu_1, \mu_2, \mu_3$ and φ. An alternative to the expansion (2.27) is

$$B_g(\mu, k_1, k_2; \mu_1, \mu_2) = \sum_{a=0}^{6} \sum_{b=0}^{6} \mathcal{B}_{ab}(\mu, k_1, k_2) (\mathrm{i}\,\mu_1)^a (\mathrm{i}\,\mu_2)^b\,, \tag{2.30}$$

where we used μ_2 instead of φ and $a, b = 0 \ldots 6$, which is the maximum power of μ_1, μ_2 that can arise. This factors out all the angular dependence from the functions $\mathcal{B}_{ab}(\mu, k_1, k_2)$, where $\mu = \cos\theta$, which just depend on the triangle shape (and the cosmology). Note that by explicitly including factors of i in the sum, we have only real coefficients $\mathcal{B}_{ab}$. Schematically we can visualise $\mathcal{B}_{ab}$ in matrix form, split into Newtonian and relativistic contributions as (a bullet denotes a non-zero entry, open circles denote zero entries, and dots are non-existent entries; here that means $a + b > 8$ as higher powers don't occur):

$$\mathcal{B}_{ab} \sim \underbrace{\begin{pmatrix} \bullet & \circ & \bullet & \circ & \bullet & \circ & \circ \\ \circ & \bullet & \circ & \bullet & \circ & \bullet & \circ \\ \bullet & \circ & \bullet & \circ & \bullet & \circ & \bullet \\ \circ & \bullet & \circ & \bullet & \circ & \bullet & \cdot \\ \bullet & \circ & \bullet & \circ & \bullet & \cdot & \cdot \\ \circ & \bullet & \circ & \bullet & \cdot & \cdot & \cdot \\ \circ & \circ & \bullet & \cdot & \cdot & \cdot & \cdot \end{pmatrix}}_{\text{Newtonian}} + \underbrace{\begin{pmatrix} \bullet & \bullet & \bullet & \bullet & \bullet & \bullet & \bullet \\ \bullet & \bullet & \bullet & \bullet & \bullet & \bullet & \bullet \\ \bullet & \bullet & \bullet & \bullet & \bullet & \bullet & \circ \\ \bullet & \bullet & \bullet & \bullet & \bullet & \circ & \cdot \\ \bullet & \bullet & \bullet & \bullet & \circ & \cdot & \cdot \\ \bullet & \bullet & \bullet & \circ & \cdot & \cdot & \cdot \\ \bullet & \bullet & \circ & \cdot & \cdot & \cdot & \cdot \end{pmatrix}}_{\text{Relativistic}} . \tag{2.31}$$

(Note that the matrix row and column labelling start at $a, b = 0, 0$ for the top left element.) Thus, the Newtonian contributions always have $a + b = \text{even} \leq 8$, contributing only to the real part of B_g, while there are relativistic contributions present for all $a + b \leq 7$. When $a + b$ is odd, this implies an imaginary component to the full bispectrum.

In terms of the powers of $\mathcal{H}/k$ involved, we can visualise the maximum powers that appear in matrix form as follows:

$$\mathcal{B}_{ab} \sim \begin{pmatrix} k^{-8} & k^{-7} & k^{-6} & k^{-5} & k^{-4} & k^{-3} & k^{-2} \\ k^{-7} & k^{-6} & k^{-5} & k^{-4} & k^{-3} & k^{-2} & k^{-1} \\ k^{-6} & k^{-5} & k^{-4} & k^{-3} & k^{-2} & k^{-1} & k^{0} \\ k^{-5} & k^{-4} & k^{-3} & k^{-2} & k^{-1} & k^{0} & \cdot \\ k^{-4} & k^{-3} & k^{-2} & k^{-1} & k^{0} & \cdot & \cdot \\ k^{-3} & k^{-2} & k^{-1} & k^{0} & \cdot & \cdot & \cdot \\ k^{-2} & k^{-1} & k^{0} & \cdot & \cdot & \cdot & \cdot \end{pmatrix} . \tag{2.32}$$

As in the matrix (2.31), the matrix row and column labelling in (2.32) starts at $(a, b) = (0, 0)$. We see that higher powers n of $(\mathcal{H}/k)^n$ appear for lower $a + b$. Newtonian contributions are all $(\mathcal{H}/k)^0$. Each element has only odd powers of $\mathcal{H}/k$ if $a + b$ is odd, and similarly only even powers if $a + b$ is even.

The advantage of writing the bispectrum in this form is that we can derive analytic formulas for the multipoles. We need to find

$$\begin{aligned} B_{\ell m} &= \int \mathrm{d}\Omega \; B_g Y^*_{\ell m} \\ &= \sum_{a,b} \mathcal{B}_{ab} X^{ab}_{\ell m} \,, \end{aligned} \tag{2.33}$$

where

$$X^{ab}_{\ell m} = \int_0^{2\pi} \mathrm{d}\varphi \int_{-1}^{1} \mathrm{d}\mu_1 \, (\mathrm{i}\,\mu_1)^a (\mathrm{i}\,\mu_2)^b \, Y^*_{\ell m}(\mu_1, \varphi). \tag{2.34}$$

To do this we use the identity, derived in appendix REF APPENDIX WITH SUM DERIVATION, for $m \geq 0$,

$$\begin{aligned} X^{ab}_{\ell m} = 2^{\ell+m-1} \mathrm{i}^{\,a+b+m} \sqrt{\frac{\pi(2\ell+1)(\ell-m)!}{(\ell+m)!}} \\ \times \sum_{p=m}^{\frac{1}{2}(b+m)} \sum_{q=m}^{\ell} \frac{[1+(-1)^{a+b+q}]\, b! \, \cos^{b+m-2p}\theta \sin^{2p-m}\theta}{4^p (b+m-2p)!(\ell-q)!(p-m)!(q-m)!} \frac{\Gamma[\frac{1}{2}(q+\ell+1)]}{\Gamma[\frac{1}{2}(q-\ell+1)]} \frac{\Gamma[\frac{1}{2}(a+b+q-2p+1}{\Gamma[\frac{1}{2}(a+b+q+3)]} \end{aligned} \tag{2.35}$$

for $m \leq b$ and zero otherwise. For $m < 0$, the result follows a similar pattern, using the simple relation $X^{ab}_{\ell -m} = (-1)^{a+b+m} X^{ax'b*}_{\ell m}$, see appendix REF DERIVATION SUM APPENDIX.

The resulting expressions for $B_{\ell m}$ are rather massive, in part because the cyclic permutations become mixed together, so we do not present them here. We can visualise these in matrix form split into their Newtonian and relativistic contributions:

$$B_{\ell m} = \underbrace{\begin{pmatrix} \bullet & \cdot & \cdot & \cdot & \cdot & \cdot & \cdot & \cdot & \cdot \\ \circ & \circ & \cdot & \cdot & \cdot & \cdot & \cdot & \cdot & \cdot \\ \bullet & \bullet & \bullet & \cdot & \cdot & \cdot & \cdot & \cdot & \cdot \\ \circ & \circ & \circ & \circ & \cdot & \cdot & \cdot & \cdot & \cdot \\ \bullet & \bullet & \bullet & \bullet & \bullet & \cdot & \cdot & \cdot & \cdot \\ \circ & \circ & \circ & \circ & \circ & \circ & \cdot & \cdot & \cdot \\ \bullet & \bullet & \bullet & \bullet & \bullet & \bullet & \bullet & \cdot & \cdot \\ \circ & \circ & \circ & \circ & \circ & \circ & \circ & \circ & \cdot \\ \bullet & \bullet & \bullet & \bullet & \bullet & \bullet & \bullet & \circ & \circ \end{pmatrix}}_{\text{Newtonian}} + \underbrace{\begin{pmatrix} \bullet & \cdot & \cdot & \cdot & \cdot & \cdot & \cdot & \cdot & \cdot \\ \bullet & \bullet & \cdot & \cdot & \cdot & \cdot & \cdot & \cdot & \cdot \\ \bullet & \bullet & \bullet & \cdot & \cdot & \cdot & \cdot & \cdot & \cdot \\ \bullet & \bullet & \bullet & \bullet & \cdot & \cdot & \cdot & \cdot & \cdot \\ \bullet & \bullet & \bullet & \bullet & \bullet & \cdot & \cdot & \cdot & \cdot \\ \bullet & \bullet & \bullet & \bullet & \bullet & \bullet & \cdot & \cdot & \cdot \\ \bullet & \bullet & \bullet & \bullet & \bullet & \bullet & \bullet & \cdot & \cdot \\ \bullet & \bullet & \bullet & \bullet & \bullet & \bullet & \bullet & \circ & \cdot \\ \circ & \circ & \circ & \circ & \circ & \circ & \circ & \circ & \circ \end{pmatrix}}_{\text{Relativistic}} . \tag{2.36}$$

Again, the matrix indices start at $(0,0)$ in the top left, $(\ell, m) = (0,0)$. In the ma-

trix (2.36), consistent with previous matrix visualisations, a closed bullet represents a non-zero entry, while an open circle denotes a vanishing entry. The dots denote the non-existent elements of the matrix, here they are matrix elements where $m > \ell$ and hence do not exist. So, the Newtonian bispectrum only induces even multipoles up to and including $\ell = 8$, while the relativistic part induces even and odd multipoles up to $\ell = 7$ with multipoles higher than $\ell = 8$ vanishing exactly. Both the Newtonian and the relativistic part terminate at $m = \pm 6$, because $m \leq b \leq 6$, as can be seen from (2.35). Note that for $m < 0$ the pattern is the same. In terms of $(\mathcal{H}/k)$ powers, the highest that appear for each ℓ is $(\mathcal{H}/k)^{8-\ell}$, while the leading contribution is $(\mathcal{H}/k)^{0 \text{ or } 1}$ if the leading contribution is Newtonian or relativistic. These powers are even (odd) if ℓ is even (odd), as explained previously along with the visualisation of the powers $\mathcal{H}/k$ in equation (2.32).

Presentation of the matrix $\mathcal{B}_{ab}$

Analysis

Here we present an analysis of the behaviour of the multipoles.

Co-linear, squeezed and equilateral limits

bob

Numerical results

bob

Conclusion

concl

A. First Appendix

Example of an appendix...

B. Second Appendix

Another appendix.

B.1. Appendix section

With a section...

Bibliography

Abramo L. R., Bertacca D., 2017, Physical Review D, 96

Baldauf T., Seljak U., Senatore L., 2011, JCAP, 1104, 006

Bernardeau F., Colombi S., Gaztañaga E., Scoccimarro R., 2002, Physics Reports, 367, 1248

Bertacca D., 2015, Class. Quant. Grav., 32, 195011

Bertacca D., Maartens R., Clarkson C., 2014a, JCAP, 09, 037

Bertacca D., Maartens R., Clarkson C., 2014b, JCAP, 1411, 013

Bertacca D., Raccanelli A., Bartolo N., Liguori M., Matarrese S., Verde L., 2018, Phys. Rev., D97, 023531

Bonvin C., 2014, Class. Quant. Grav., 31, 234002

Camera S., Fonseca J., Maartens R., Santos M. G., 2018, Mon. Not. Roy. Astron. Soc., 481, 1251

Celoria M., Matarrese S., 2020, Proc. Int. Sch. Phys. Fermi, 200, 179

Challinor A., Lewis A., 2011, Phys. Rev. D, 84, 043516

Clarkson C., de Weerd E. M., Jolicoeur S., Maartens R., Umeh O., 2019, Monthly Notices of the Royal Astronomical Society, 486, L101

Desjacques V., Jeong D., Schmidt F., 2018, Phys. Rept., 733, 1

Di Dio E., Seljak U., 2019, JCAP, 04, 050

Di Dio E., Durrer R., Marozzi G., Montanari F., 2014, JCAP, 12, 017

Di Dio E., Perrier H., Durrer R., Marozzi G., Moradinezhad Dizgah A., Noreña J., Riotto A., 2017, JCAP, 1703, 006

Di Dio E., Durrer R., Maartens R., Montanari F., Umeh O., 2019, JCAP, 1904, 053

Fonseca J., Maartens R., Santos M. G., 2018, Mon. Not. Roy. Astron. Soc., 479, 3490

Hall A., Bonvin C., 2017, Phys. Rev. D, 95, 043530

Jeong D., Komatsu E., 2009, Astrophys. J., 703, 1230

Jeong D., Schmidt F., Hirata C. M., 2012, Physical Review D, 85

Jolicoeur S., Umeh O., Maartens R., Clarkson C., 2017, JCAP, 09, 040

Jolicoeur S., Umeh O., Maartens R., Clarkson C., 2018, JCAP, 03, 036

Jolicoeur S., Allahyari A., Clarkson C., Larena J., Umeh O., Maartens R., 2019, JCAP, 03, 004

Kaiser N., 1987, Mon. Not. Roy. Astron. Soc., 227, 1

Karagiannis D., Lazanu A., Liguori M., Raccanelli A., Bartolo N., Verde L., 2018, Monthly Notices of the Royal Astronomical Society, 478, 13411376

Lewis A., Challinor A., Lasenby A., 2000, Astrophys. J., 538, 473

Maartens R., Jolicoeur S., Umeh O., De Weerd E. M., Clarkson C., Camera S., 2020, JCAP, 2020, 065065

McDonald P., 2009, JCAP, 11, 026

Nan Y., Yamamoto K., Hikage C., 2018, JCAP, 07, 038

Raccanelli A., Bertacca D., Jeong D., Neyrinck M. C., Szalay A. S., 2018, Phys. Dark Univ., 19, 109

Scoccimarro R., Couchman H. M. P., Frieman J. A., 1999, The Astrophysical Journal, 517, 531540

Sugiyama N. S., Saito S., Beutler F., Seo H.-J., 2018, Monthly Notices of the Royal Astronomical Society, 484, 364384

Tansella V., Bonvin C., Durrer R., Ghosh B., Sellentin E., 2018, JCAP, 03, 019

Tellarini M., Ross A. J., Tasinato G., Wands D., 2016, Journal of Cosmology and Astroparticle Physics, 2016, 014014

Umeh O., Maartens R., Santos M., 2016, JCAP, 03, 061

Umeh O., Jolicoeur S., Maartens R., Clarkson C., 2017, JCAP, 03, 034

Umeh O., Koyama K., Maartens R., Schmidt F., Clarkson C., 2019, JCAP, 1905, 020

Verde L., Heavens A. F., Matarrese S., Moscardini L., 1998, Monthly Notices of the Royal Astronomical Society, 300, 747756

Villa E., Rampf C., 2016, JCAP, 1601, 030

Yankelevich V., Porciani C., 2019, Mon. Not. Roy. Astron. Soc., 483, 2078

Yoo J., Zaldarriaga M., 2014, Phys. Rev. D, 90, 023513

List of Figures

1.1. The absolute value of the bispectrum dipole at $z = 1$ as a function of triangle size, in the flattened (Left, $\theta = 2°$, for intensity mapping bias) and squeezed (Right, $\theta = 178°$, for Euclid-like bias) configurations, with k_3 as the horizontal axis. Red is the $m = 0$ part and blue is $m = \pm 1$. Dashed (and dotted) lines show up to the $O(\mathcal{H}/k)$ terms considered analytically here, while solid lines indicate larger-scale contributions. For reference the monopole is in black, with the dotted line the Newtonian part. (The zero-crossing in the monopole for the squeezed case is a result of the tidal bias.) 7

1.2. (Left) We show the dipoles as a function of θ with a bias appropriate for a Euclid-like survey, for $k_1 = k_2 = 0.01\,\mathrm{Mpc}^{-1}$. The left of the plot corresponds to the flattened case where the $m = 0$ (red) dipole reaches 10% of the monopole. (Right) We show the IM signal with $k_1 = k_2 = 0.1\,\mathrm{Mpc}^{-1}$ versus the long mode k_3. Except for very long modes $\theta \approx \pi$, our $O(\mathcal{H}/k)$ truncation is a very good approximation in these examples. 8

2.1. Overview of the relevant vectors and angles for the Fourier-space bispectrum. 18

List of Tables